JOURNAL OF
SYNCHROTRON
RADIATION

ISSN 1600-5775

Received 5 August 2016
Accepted 4 January 2017

Edited by P. A. Pianetta, SLAC National Accelerator Laboratory, USA

Keywords: X-ray and γ-ray detectors; CdZnTe detectors; travelling heater method; gold electroless contact; high flux; digital pulse shape analysis; energy-resolved photon-counting detectors.

Development of new CdZnTe detectors for room-temperature high-flux radiation measurements

Leonardo Abbene,[a]* Gaetano Gerardi,[a] Giuseppe Raso,[a] Fabio Principato,[a] Nicola Zambelli,[b] Giacomo Benassi,[b] Manuele Bettelli[c] and Andrea Zappettini[c]

[a]Dipartimento di Fisica e Chimica, University of Palermo, Viale delle Scienze, Edificio 18, Palermo 90128, Italy, [b]Due2Lab srl, Via Paolo Borsellino 2, Scandiano, Reggio Emilia 42019, Italy, and [c]IMEM/CNR, Parco Area delle Scienze 37/A, Parma 43100, Italy. *Correspondence e-mail: leonardo.abbene@unipa.it

Recently, CdZnTe (CZT) detectors have been widely proposed and developed for room-temperature X-ray spectroscopy even at high fluxes, and great efforts have been made on both the device and the crystal growth technologies. In this work, the performance of new travelling-heater-method (THM)-grown CZT detectors, recently developed at IMEM-CNR Parma, Italy, is presented. Thick planar detectors (3 mm thick) with gold electroless contacts were realised, with a planar cathode covering the detector surface (4.1 mm × 4.1 mm) and a central anode (2 mm × 2 mm) surrounded by a guard-ring electrode. The detectors, characterized by low leakage currents at room temperature (4.7 nA cm^{-2} at 1000 V cm^{-1}), allow good room-temperature operation even at high bias voltages (>7000 V cm^{-1}). At low rates (200 counts s^{-1}), the detectors exhibit an energy resolution around 4% FWHM at 59.5 keV (^{241}Am source) up to 2200 V, by using commercial front-end electronics (A250F/NF charge-sensitive preamplifier, Amptek, USA; nominal equivalent noise charge of 100 electrons RMS). At high rates (1 Mcounts s^{-1}), the detectors, coupled to a custom-designed digital pulse processing electronics developed at DiFC of University of Palermo (Italy), show low spectroscopic degradations: energy resolution values of 8% and 9.7% FWHM at 59.5 keV (^{241}Am source) were measured, with throughputs of 0.4% and 60% at 1 Mcounts s^{-1}, respectively. An energy resolution of 7.7% FWHM at 122.1 keV (^{57}Co source) with a throughput of 50% was obtained at 550 kcounts s^{-1} (energy resolution of 3.2% at low rate). These activities are in the framework of an Italian research project on the development of energy-resolved photon-counting systems for high-flux energy-resolved X-ray imaging.

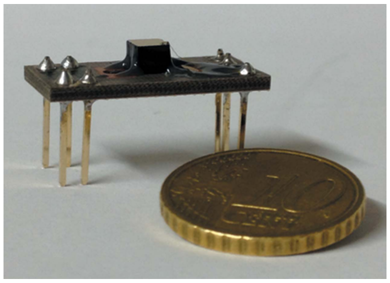

1. Introduction

In the last decade, great efforts have been made in the development of imaging arrays, with single-photon-counting and energy-resolving capabilities, for colour/spectroscopic X-ray imaging (Fredenberg *et al.*, 2010; Norlin *et al.*, 2008; Taguchi & Iwanczyk, 2013; Tomita *et al.*, 2004), opening new perspectives for applications within the fields of diagnostic medicine, synchrotron applications, non-destructive testing and security screening. Energy-resolved photon-counting (ERPC) arrays are typically based on high-Z and wide-band-gap direct-conversion compound semiconductors (gallium arsenide, cadmium telluride, cadmium zinc telluride) (Abbene *et al.*, 2015; Barber *et al.*, 2015; Iwanczyk *et al.*, 2009; Szeles *et al.*, 2008; Veale *et al.*, 2014), which ensure room-temperature operation and higher detection efficiency (up to 140 keV) than the traditional semiconductor detectors (silicon, germanium) (Del Sordo *et al.*, 2009; Owens & Peacock, 2004; Takahashi & Watanabe, 2001). Silicon drift detectors, invented in 1984 by

https://doi.org/10.1107/S1600577517000194

Gatti and Rehak (Gatti & Rehak, 1984; Gatti *et al.*, 1984), are currently proposed for room-temperature spectroscopic X-ray imaging, representing the best solution up to 20 keV (Bertuccio *et al.*, 2015). Despite their excellent energy resolution and high detection efficiency up to 140 keV, few ERPC prototypes, based on high-purity germanium (HPGe) detectors, have been developed, mainly due to their cumbersome cryogenic cooling (liquid and mechanical coolers) (Johnson *et al.*, 2015; Campbell *et al.*, 2013).

Owing to the high-flux conditions of several imaging applications ($>10^6$ photons mm^{-2} s^{-1}), the development of high-resolution ERPC systems must take into account several critical issues. Dead-time, pile-up, charge-sharing and radiation-induced polarization distortions are the main drawbacks. The mitigation of the first three distortions is, generally, the main task of the readout electronics (pulse mode electronics) and important results are obtained through both analog (Barber *et al.*, 2015; Iwanczyk *et al.*, 2009; Taguchi *et al.*, 2010) and digital approaches (Abbene *et al.*, 2015; Brambilla *et al.*, 2013). High-flux radiation-induced polarization phenomena (Bale & Szeles, 2008; Sellin *et al.*, 2010) mainly depend on the characteristics of the detectors, and high bias voltage operation and good charge transport properties (mobility-lifetime products of holes and electrons) are required.

Among the compound semiconductors, cadmium zinc telluride (CdZnTe or CZT) detectors are primary candidates for the development of ERPC systems, able to ensure room-temperature operation, good energy resolution and high detection efficiency in thicknesses of a few millimeters (Del Sordo *et al.*, 2009; Owens, 2006; Takahashi & Watanabe, 2001; Iniewski, 2014). ERPC systems based on pixelated CZT detectors offer modest energy resolution at high fluxes ($>10^6$ photons mm^{-2} s^{-1}), typically of the order of 10–20% at 60 keV (Barber *et al.*, 2015; Brambilla *et al.*, 2009; Baumer *et al.*, 2008; Greenberg *et al.*, 2016), and advances in both the CZT crystal growth and the device technology are required. Great efforts have been made on the development of CZT detectors based on spectroscopic grade crystals and characterized by electrical contacts (quasi-ohmic contacts) with low leakage currents (Auricchio *et al.*, 2011; Bell *et al.*, 2015; Chen *et al.*, 2007; Park *et al.*, 2008; Chaudhuri *et al.*, 2014; Szeles *et al.*, 2008; Abbene *et al.*, 2016; Zappettini *et al.*, 2009). Currently, CZT crystals with excellent charge transport properties ($\mu_e\tau_e > 10^{-2}$ cm^2 V^{-1}) are produced by a Canadian company (Redlen Technologies, Victoria BC, Canada) using the travelling heater method (THM) growth technique (Awadalla *et al.*, 2014; Chen *et al.*, 2007). THM-grown CZT detectors, despite their excellent charge transport properties, generally operate at moderate electric fields (<2000 V cm^{-1}) (Awadalla *et al.*, 2014; Chen *et al.*, 2007), thus limiting the reduction of high-flux polarization and charge-sharing effects in pixelated detectors.

Recently, within an Italian research collaboration (DiFC of University of Palermo and IMEM-CNR of Parma), we proposed to develop ERPC prototypes, based on CZT pixel detectors and digital pulse processing (DPP) electronics, for high-flux energy-resolved X-ray imaging applications (1–140 keV). In this framework, we developed, as a first step, some CZT prototypes, with planar electrode structures, to investigate their high-flux spectroscopic performance.

In this work, we will present the results of a full characterization of the electrical, charge transport and spectroscopic properties of new THM-grown CZT detectors with quasi-ohmic contacts, recently developed at IMEM-CNR, Parma, Italy. The detectors, based on CZT crystals provided by Redlen Technologies, are characterized by low leakage currents allowing high bias voltage operation (>7000 V cm^{-1}) even at room temperature. The main transport mechanisms of the new devices were investigated by modelling the measured *I*–*V* curves (under reverse bias voltages) with the interfacial-layer–thermionic-diffusion (ITD) model (Bolotnikov *et al.*, 2002; Wu, 1982). An accurate characterization of the spectroscopic response of the detectors, at both low (200 counts s^{-1}) and high (up to 1 Mcounts s^{-1}) rates, to monochromatic X-ray and γ-ray sources (^{109}Cd, ^{241}Am and ^{57}Co) was performed by using custom-designed digital readout electronics, developed at DiFC of University of Palermo (Italy). The readout electronics are able to continuously digitize and process the signals from the detectors (*i.e.* the preamplifier output signals) and perform a fine pulse shape and height analysis even at high fluxes.

2. Materials and methods

2.1. Detectors

The detectors, fabricated by IMEM-CNR (Parma, Italy; http://www.imem.cnr.it) and Due2Lab srl (Reggio Emilia, Italy; http://www.due2lab.com), are based on CZT crystals (4.1 mm × 4.1 mm × 3 mm), grown by Redlen Technologies (Victoria BC, Canada; http://redlen.ca) using the THM technique (Awadalla *et al.*, 2014; Chen *et al.*, 2007, 2008). The cathode is a planar electrode covering the detector surface (4.1 mm × 4.1 mm) and the anode surface is characterized by a central electrode (2 mm × 2 mm) surrounded by a guard-ring electrode (Fig. 1). The width of the guard-ring is 950 µm and the gap between the electrodes is 50 µm. As shown in Fig. 1, the detectors were bonded with 50 µm Au wires onto a high-resistivity printed circuit board.

Gold electroless contacts were realised on both the anode and the cathode of the detectors. A 4% $AuCl_3$ methanol solution, with a deposition time of 1 min at 25°C, was used. The anode pattern (guard-ring and pixel) was obtained by photolithography process and the passivation procedure was performed with 10% of H_2O_2 for 5 min, in order to reduce the surface leakage currents. THM-grown CZT detectors with gold electroless contacts (CZT B) are widely fabricated at IMEM-CNR and characterized by electrical and spectroscopic properties in agreement with the literature (Abbene *et al.*, 2016; Turturici *et al.*, 2016). Recently, THM-grown CZT detectors with a new gold electroless contact technique (CZT A) have been developed at IMEM-CNR. These new devices, characterized by very low leakage currents, allow high bias voltage operation (>7000 V cm^{-1}) even at room

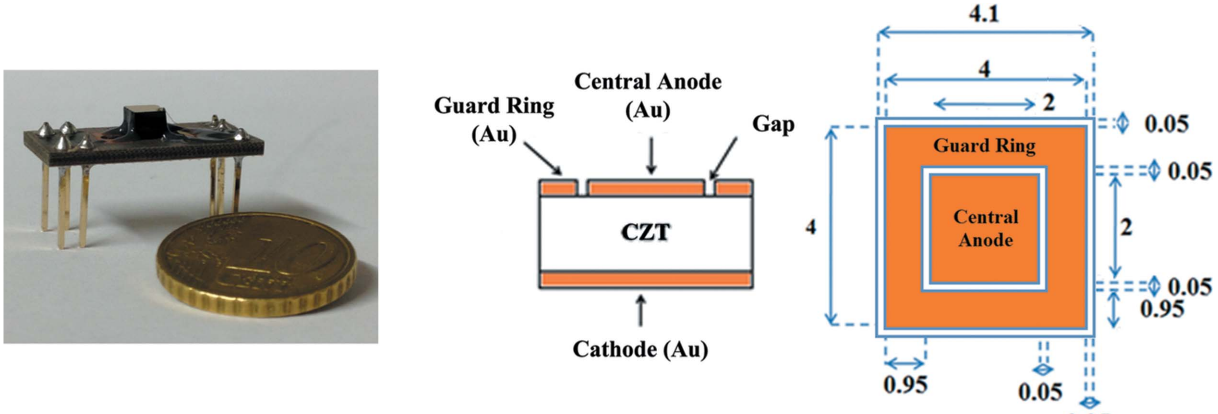

(*a*) (*b*)

Figure 1
(*a*) The new 3 mm-thick THM-grown CZT detector (cathode side view). (*b*) Schematic cross-section view of the detectors and the anode electrode layout (all dimensions are expressed in millimeters).

temperature with excellent prospective for high-flux radiation measurements. Comparison between the new (CZT A) and the standard (CZT B) THM-grown CZT detectors will be presented.

2.2. Electronics

The spectroscopic performance of the detectors was measured by using standard front-end electronics. We used a commercial AC-coupled charge-sensitive preamplifier (CSP; A250F/NF with external FET SK152, Amptek, USA; http://amptek.com) with a nominal equivalent noise charge of about 100 electrons RMS. The CSP is characterized by a resistive-feedback circuit (feedback resistor, $R_{\rm f}$ = 1 GΩ; feedback capacitor, $C_{\rm f}$ = 0.25 pF) with a decay time of 250 µs.

The detectors and the CSP were mounted on a custom PCB board based on a polytetrafluoroethylene (PTFE) substrate (the distance between the detector-anode and the CSP was less than 1 cm). The PCB board was enclosed in a shielded box and the detectors were irradiated through a light-tight beryllium window.

The height analysis of the CSP output pulses was performed through custom DPP electronics, recently developed at DiFC of University of Palermo (Italy) (Abbene *et al.*, 2013; Abbene & Gerardi, 2015; Gerardi & Abbene, 2014). The DPP system, by digitizing and processing the CSP output waveforms, is able to perform an accurate pulse shape and height (PSHA) analysis (*e.g.* arrival time, pulse height and pulse shape) even at high input counting rates (ICRs). The DPP system consists of a digitizer (DT5724, 16 bit, 100 MS $\rm s^{-1}$, CAEN SpA, Italy; http://www.caen.it) and a PC, which controls all digitizing functions, the acquisition and the analysis. The pulse-processing analysis is performed by using a custom DPP firmware uploaded to the digitizer. A general overview of the method is presented below and a detailed description of the method is reported in previous works (Abbene *et al.*, 2013; Abbene & Gerardi, 2015; Gerardi & Abbene, 2014). The DPP method, as shown in Fig. 2, is based on two pipelined shaping steps: a *fast* and a *slow* PSHA. The CSP output waveforms are shaped by using the classical single delay line (SDL) shaping technique (Knoll, 2000). SDL shaping is obtained by subtracting from the original pulse its delayed and attenuated fraction. SDL shaping gives short rectangular output pulses with fast rise and fall times. Generally, two main features characterize the SDL shaping: (i) the time width of each SDL shaped pulse is well defined (delay time + CSP peaking time) and (ii) if the delay time is greater than the peaking time of the CSP pulse, the SDL shaping also preserves the leading edge (pulse height and peaking time) of each CSP output pulse. These features make SDL shaping very appealing for timing and PSHA at both low and high ICRs. Through the *fast* PSHA the following operations are performed:

(i) Pulse detection and time-tag triggering after fast SDL shaping with short delay time.

(ii) Pulse shape and height analysis (fast PSHA), that provides energy spectra (pulse height distributions of the fast SDL shaped pulses) with high throughputs (*i.e.* the OCR/ICR

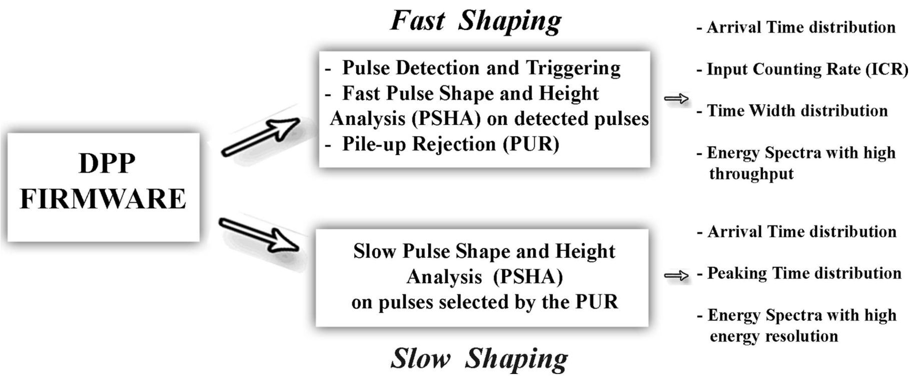

Figure 2
The main operations and output data of the digital pulse processing (DPP) system.

ratio, where OCR is the output counting rate and ICR the input counting rate); the time width (*i.e.* one of the shape-related parameters) of the SDL shaped pulses is also measured; to minimize the effects of baseline shifts in the measured spectra, the system performs a fast baseline recovery by using the running average value of a fixed number of samples preceding the SDL pulse, where no further pulses are present.

(iii) Pile-up rejection (PUR) for the slow PSHA; the PUR is used to select time windows of the CSP waveform for the slow PSHA. Each selected time window of the CSP waveform is termed *Snapshot*, while the width of this window, user-chosen, is termed *Snapshot Time* (ST). If two detected fast SDL pulses are within ST/2 of each other, then neither pulse will be selected, *i.e.* a pulse is accepted if it is not preceded and not followed by another pulse in the ST/2 time window periods.

The main feature of the *slow* PSHA is that the processing is performed on each PUR selected *Snapshot*, containing only one CSP pulse. The energy resolution strongly depends on the ST values; as the shaping time of classic analog systems, long ST values give better energy resolution. Through the *slow* PSHA, the system is able to provide, for each selected CSP pulse, the following results:

(i) Trigger time obtained in the fast PSHA.

(ii) Peaking time (one of the shape related parameters) of each isolated CSP pulse after the slow SDL shaping (*i.e.* with a long delay time).

(iii) Pulse height of each isolated CSP pulse after the slow SDL shaping, followed by an automatic baseline restorer and a trapezoidal filtering.

The shape related parameters (the *peaking time* of the slow shaped pulses and the *time width* of the fast shaped pulses) and their relation with the pulse height are very helpful for improving the detector performance. Pulse shape discrimination techniques were successfully used in our previous works (Abbene & Gerardi, 2011; Abbene *et al.*, 2015) to minimize incomplete charge collection effects, pile-up and charge sharing.

Both the time width of the pulses from the fast shaping and the ST are dead-times for the system with a well defined modelling (paralyzable dead-time). In particular, the fast analysis is characterized by a dead-time (*fast dead time*) equal to the mean value of the time widths of the fast shaped pulses; while, the dead-time of the slow analysis is equal to ST minus the fast dead-time (Abbene *et al.*, 2015). As well highlighted in a previous work, the true ICR can be estimated or obtained from an exponential best fit of the measured time-interval distribution of the fast shaped pulses, or by applying the inversion of the throughput formula of the fast analysis.

2.3. Experimental procedures

The electrical properties (current–voltage curves) of the detectors were measured by using a high-voltage source meter, Keithley 2410, which provides the detector bias voltage, and a source-measure unit, Keithley 236, configured as electrometer. The guard ring of the detectors is held at zero potential to prevent surface leakage currents.

To investigate the spectroscopic performance of the detectors, we used X-ray and γ-ray calibration sources (^{109}Cd: 22.1, 24.9 and 88.1 keV; ^{241}Am: 59.5 and 26.3 keV; ^{57}Co: 122.1 and 136.5 keV). The ^{57}Co energy spectra also feature the W fluorescent lines produced in the tungsten source backing ($K_{\alpha 1}$ = 59.3 keV, $K_{\alpha 2}$ = 58.0 keV, $K_{\beta 1}$ = 67.2 keV, $K_{\beta 3}$ = 66.9 keV). We used two different ^{241}Am sources: (i) a low-activity source (0.1 MBq) also emitting the Np L X-ray lines (13–21 keV), and (ii) a high-activity source (370 MBq) where the Np L X-ray lines are shielded by the source holder. The 14 keV γ-line of the ^{57}Co source is also shielded by the source holder. To obtain different ICRs of the impinging photons on the detectors (through the cathode surface), we changed the solid angle subtended by the detectors, *i.e.* the distance from the sources to the detectors.

3. Measurements and results

3.1. Electrical and charge transport properties

Fig. 3 shows the current–voltage (I–V) characteristics of the new THM-grown CZT detector (CZT A), measured at different temperatures (from T = 40°C to T = 15°C, with temperature steps of 5°C). The behaviour of the I–V curves is typical of the quasi-ohmic Au/CZT/Au contacts, *i.e.* of a metal–semiconductor–metal device with two back-to-back Schottky barriers (Bolotnikov *et al.*, 2002; Marchini *et al.*, 2009). As clearly visible in the figure, the detector is characterized by very low leakage currents in the reverse bias region: 4.7 nA cm^{-2} at 300 V (1000 V cm^{-1}) at T = 25°C and 1.4 nA cm^{-2} at T = 15°C. Moreover, the detector ensures moderate leakage currents, at room temperature (T = 25°C), even at high bias voltages: 93 nA cm^{-2} at 2000 V

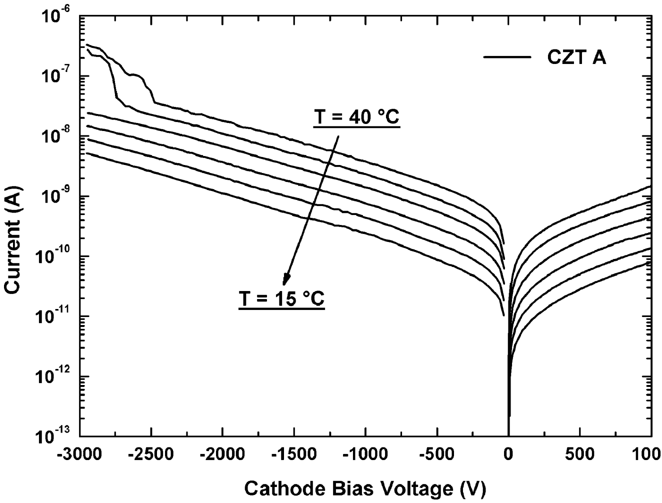

Figure 3
I–V curves of the new THM-grown CZT detector (CZT A) measured at different temperatures (from T = 40°C to T = 15°C, with temperature steps of 5°C). Moderate leakage current of 370 nA cm^{-2} (T = 25°C) was measured even at very high electric field of 10000 V cm^{-1}. The area of the anode electrode is equal to 4 mm^2.

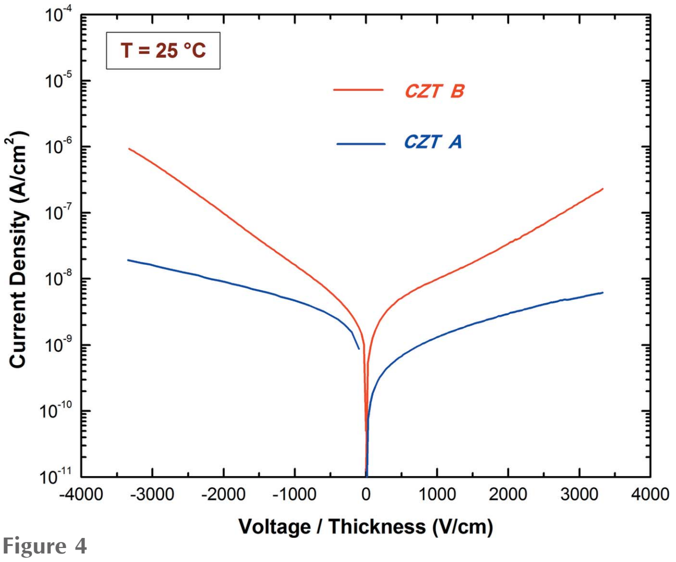

Figure 4
Measured I–V curves of the CZT A and CZT B detectors at T = 25°C. Despite the leakage current values of CZT B being in agreement with the literature (Awadalla *et al.*, 2014), they are higher than those of CZT A.

(6700 V cm^{-1}) and 370 nA cm^{-2} at 3000 V (10000 V cm^{-1}). Fig. 4 shows an interesting comparison between the I–V curves of the CZT A and CZT B detectors. The CZT B detector is characterized by leakage current values (16 nA cm^{-2} at 1000 V cm^{-1} at T = 25°C) in agreement with the literature (Awadalla *et al.*, 2014; Bell *et al.*, 2015; Chen *et al.*, 2007), but higher than the CZT A ones.

To better understand these experimental results, we described the measured I–V curves (under reverse bias voltage) through the ITD model (Bolotnikov *et al.*, 2002; Wu, 1982). Fig. 5 shows the measured I–V curves, under reverse bias voltages, of both detectors with the description of the main transport mechanisms. For the CZT B detector, in agreement with the ITD model, the bulk resistivity dominates at low voltages (<0.5 V). At intermediate voltages (<2 V) the I–V curve follows Ohm's law, but, due to the depletion of the CZT crystal, the specific resistivity is higher than the real bulk resistivity. Then the diffusion-thermionic emission, which depends on the interfacial layer between the contact and CZT material, dominates. In particular, this interfacial layer, due to the surface treatments of the crystals during the detector fabrication process, reduces the current by a factor θ_n (*i.e.* the transmission coefficient through the interfacial layer). In this range, at low voltages the diffusion-limited current regime dominates, while at higher voltages the exponential rise of the current is dominated by the barrier lowering of the thermionic emission. Finally, at very high voltages both I–V curves follow a power law due to the space charge limited current transport mechanism. Concerning the new CZT detector (CZT A), the I–V curve is characterized by the formation of the depletion region even at low voltages (< 1 V), precluding the possibility to estimate the bulk resistivity. The I–V curve is characterized by a shift through the voltage range, allowing low leakage currents even at high voltages. Indeed, also the diffusion and thermionic emission mechanisms occur at higher voltages compared with the CZT B detector. In particular, the thermionic emission occurs at about 200 V for CZT A, while it occurs at about 30 V for CZT B.

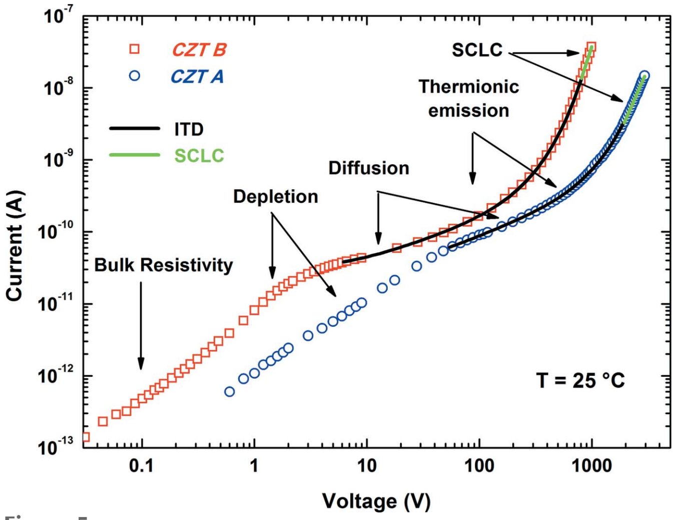

Figure 5
Measured reverse I–V curves of the CZT A and CZT B detectors at T = 25°C. The main transport mechanisms are also highlighted.

In order to perform a quantitative interpretation of these differences, we applied the ITD model to the measured I–V curves. At voltages where the detectors are fully depleted and the diffusion and the thermionic emission mechanisms dominate, the current density $J_{\rm R}$ as a function of the reverse voltage $V_{\rm R}$ can be expressed as (Turturici *et al.*, 2016)

$$J_{\rm R} = \left\{ \frac{C_0}{1+\left[C_4/(C_5+V_{\rm R})\right]} \right\} \exp\left(\frac{qC_2V_{\rm R}}{kT}\right), \qquad (1)$$

with

$$C_0 = \theta_n A^* T^2 \exp\left(-\frac{q\varphi_{\rm B0}}{kT}\right),$$
$$C_2 = 1-\frac{\varepsilon_{\rm i}}{\varepsilon_{\rm i}+2q\delta_{\rm i}D_{\rm s}},$$
$$C_4 = \frac{\theta_n L V_{\rm t}}{\mu}, \qquad C_5 = V_{\rm RT} - E_0 L,$$

where A^* is the effective Richardson constant, θ_n is the transmission coefficient through the interfacial layer, $\varphi_{\rm B0}$ is the Au/CZT barrier height under thermal equilibrium conditions, $\varepsilon_{\rm i}$ and $\delta_{\rm i}$ are the permittivity and the thickness of the interfacial layer, $D_{\rm s}$ is the density of surface states per unit energy and area, μ is the electron mobility, $V_{\rm t}$ is the thermal velocity, $V_{\rm RT}$ is the voltage required to fully deplete the detector, and E_0 is the electric field strength at the anode when the cathode is at $V_{\rm RT}$.

By using the fitting function (1), we estimated the C_0 values for both CZT detectors. We extracted the values of barrier height $\varphi_{\rm B0}$ (under thermal equilibrium conditions) from the slope of the Arrhenius plot $\ln(C_0/T^2)$ *versus* $1/kT$, as shown in Fig. 6. Despite the differences between the I–V curves of the two CZT detectors, they are characterized by similar $\varphi_{\rm B0}$ values. Further helpful results, reported in Table 1, can allow

Table 1
Au/CZT barrier height φ_{B0} under thermal equilibrium, transmission coefficient θ_n, C_2 and C_5 parameters, estimated by applying the ITD model [equation (1)] to the reverse *I–V* curves of the CZT detectors at T = 25°C.

Sample	φ_{B0} (eV)	θ_n	C_2	C_5
CZT A	0.92 ± 0.01	0.063	4.0×10^{-5}	10.6
CZT B	0.90 ± 0.01	0.016	1.5×10^{-4}	20.7

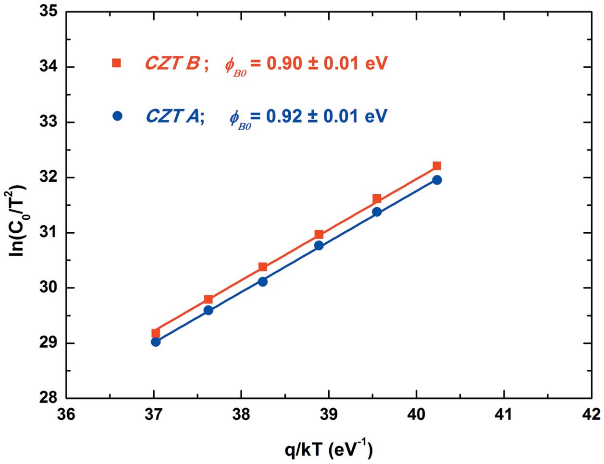

Figure 6
Experimental Arrhenius plot of the parameter C_0, estimated through a fitting of the measured reverse *I–V* curves with equation (1). Despite the differences between the *I–V* curves of the two CZT detectors, they are characterized by similar φ_{B0} values.

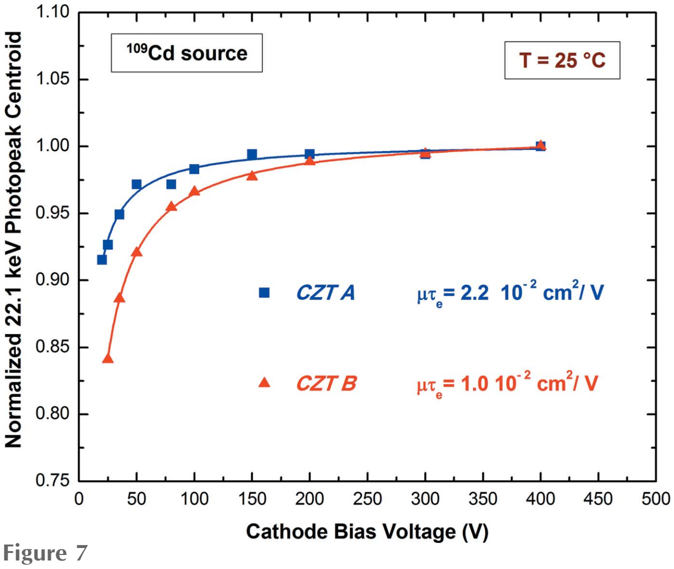

Figure 7
Normalized 22.1 keV photopeak centroid (*i.e.* the charge collection efficiency) at various cathode bias voltages for both CZT detectors. The experimental points are fitted with the simplified Hecht equation (Sellin *et al.*, 2005). The estimated $\mu_e\tau_e$ values are in agreement with the typical values presented in the literature (Awadalla *et al.*, 2014; Chen *et al.*, 2007, 2008). The ^{109}Cd spectra were measured using the slow PSHA with ST = 9 µs (optimal ST value).

us to understand the differences between electrical properties of the two CZT detectors.

The values of the transmission coefficient θ_n were obtained from the C_4 values after fitting, by assuming V_t = 8.5 × 10^6 cm s^{-1} and μ = 1000 cm^2 V^{-1} s^{-1}. The parameter C_2 depends on both the thickness of the interfacial layer and the density of surface states D_s. The Schottky barrier height φ_R depends on the barrier lowering due to the voltage drop across the interfacial layer by

$$\varphi_R = \varphi_{B0} - C_2 V. \tag{2}$$

From the results of Table 1, only the C_2 values have a marked difference between the two detectors. Due to the dependence of C_2 on D_s, the new CZT detector is characterized by lower density of surface states than for CZT B. Low D_s values cause an increasing of the Schottky barrier height and, therefore, low leakage current values.

Moreover, the lower effect of the interfacial layer in the CZT A detector (pointed out by the higher θ_n value than the CZT B one) explains how the leakage current is diffusion-limited up to higher voltages than for CZT B.

The charge transport properties of the detectors were also investigated through the estimation of the mobility-lifetime product of the electrons $\mu_e\tau_e$. To evaluate $\mu_e\tau_e$, we irradiated the detectors from the cathode side, by using the 22.1 keV line of the ^{109}Cd source, and the energy spectra at different bias voltages were measured. The measured charge collection efficiencies of two samples at 22.1 keV *versus* the bias voltage are reported in Fig. 7. The experimental points are fitted with the simplified Hecht equation (Sellin *et al.*, 2005). The estimated $\mu_e\tau_e$ values are in agreement with the typical values presented in the literature (Awadalla *et al.*, 2014; Chen *et al.*, 2007, 2008).

In the following sections, we will show how these properties and differences will be crucial in the spectroscopic performance of the CZT detectors, especially at high fluxes.

3.2. Room-temperature spectroscopic response at low and high rates

The time-stability of the detectors, at low rates (ICR = 200 counts s^{-1}), was first investigated. ^{241}Am and ^{57}Co spectra were measured, by using an electric field of 1500 V cm^{-1}, and both detectors showed good time-stability within a time window of 30 min, in agreement with the literature. All energy spectra were measured by using the slow PSHA with ST = 9 µs, which gives the best energy resolution values. The same low-rate performance were obtained by using an analog Gaussian shaping amplifier (model 672, Ortec, USA) with a shaping time constant of 1 µs and a multichannel analyzer (MCA 8000A, Amptek, USA). Fig. 8 shows an overview of the measured energy resolution (FWHM) at 59.5 keV (^{241}Am source) of the detectors at different bias voltages. Generally, similar low-rate performance (energy resolution around 4% at 59.5 keV) for both CZT detectors were measured, though obtained at different optimal bias voltages. These results are in agreement with the energy resolution values obtained, at low rates, by other researchers with planar CZT detectors coupled to the A250 preamplifier (Deng *et al.*, 2007). The CZT A detector allows higher bias voltage operation (>7000 V cm^{-1})

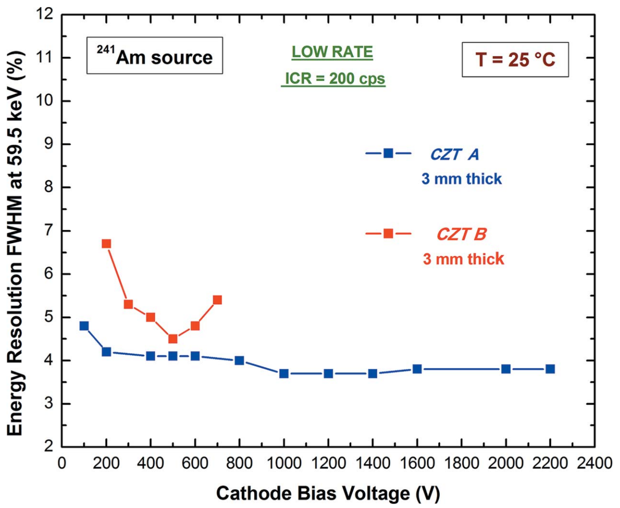

Figure 8
Energy resolution (FWHM) at 59.5 keV *versus* the bias voltage at room temperature for the CZT detectors. The spectra were measured by using the digital slow PSHA with ST = 9 µs (optimal ST value). The same low-rate results were obtained by using an analog Gaussian shaping amplifier (model 672, Ortec, USA) with a shaping time constant of 1 µs and a commercial multichannel analyser (MCA 8000A, Amptek, USA).

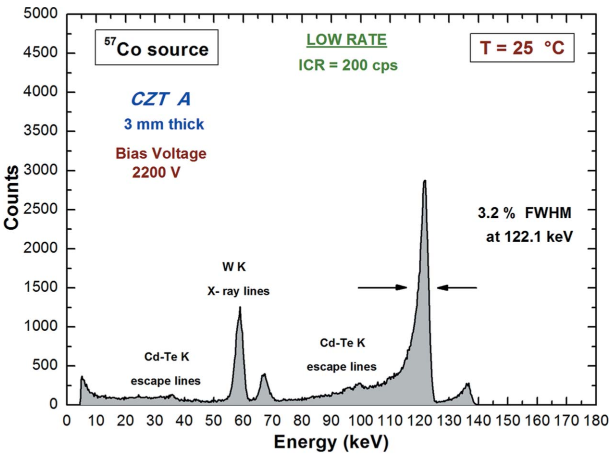

Figure 10
The measured ^{57}Co spectrum for the CZT A detector at a bias voltage of 2200 V. The spectrum was measured using the slow PSHA with ST = 9 µs. The Co γ-ray lines (122.1 and 136.5 keV), the W K X-ray lines ($K_{\alpha 1}$ = 59.3 keV, $K_{\beta 1}$ = 67.2 keV), the Cd–Te escape lines related to the 122.1 keV line (Cd K_{α} escape = 98.9 keV, Cd K_{β} escape = 96 keV, Te K_{α} escape = 93.6 keV) and the Cd–Te escape lines related to the 59.3 keV line (Cd K_{α} escape = 36.1 keV, Cd K_{β} escape = 33.2 keV, Te K_{α} escape = 31.8 keV) are clearly visible.

than CZT B ($<$2000 V cm^{-1}), in agreement with the measured electrical characteristics. Despite the best energy resolution (3.7% FWHM at 59.5 keV) for the CZT A detector obtained at voltages between 1000 V and 1400 V, we prefer to show the ^{241}Am and ^{57}Co spectra measured at the maximum bias voltage of 2200 V (7300 V cm^{-1}), characterized by similar performance and shown in Figs. 9 and 10. The maximum voltage of 2200 V was fixed by the electronic components of the bias voltage filters.

At high rates, the time-stability of the detectors was verified, within a time window of 30 min, up to 1 Mcounts s^{-1} (^{241}Am source). Fig. 11 demonstrates the time-stability of the CZT A detector (^{241}Am source) at 1 Mcounts s^{-1}. The new CZT detectors, due to their high bias voltage operation, are characterized by better high-rate performance than the standard ones, as shown in Figs. 12 and 13. The spectra of Fig. 13 were measured at the optimal bias voltages of 900 V and 2200 V for CZT B and CZT A, respectively. At high rates, the optimal bias voltages of the detectors are generally greater than the optimal bias voltage values obtained at low rates (Fig. 8). This is due to the high-flux radiation-induced polarization phenomena (Bale & Szeles, 2008; Sellin *et al.*, 2010; Szeles *et al.*, 2008), producing a degradation of the electric field within the detectors. The electric field distortions are caused

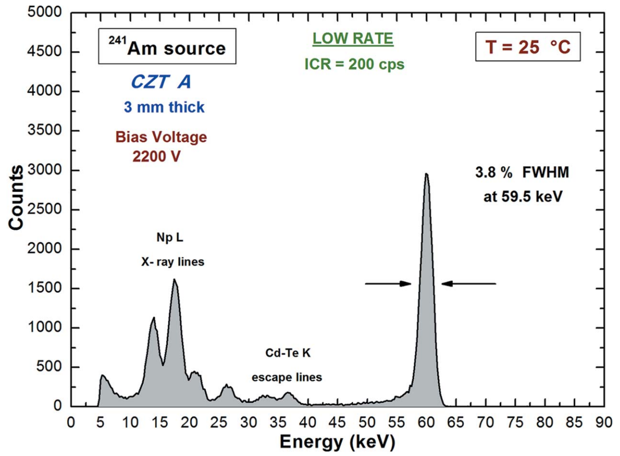

Figure 9
The measured ^{241}Am spectrum for the CZT A detector at a bias voltage of 2200 V. The spectrum was measured using the slow PSHA with ST = 9 µs. The Am γ-ray lines (59.5 and 26.3 keV), the Np L X-ray lines ($L_{\alpha 1}$ = 13.9 keV, $L_{\beta 1}$ = 17.8 keV, $L_{\gamma 2}$ = 21.1 keV) and the Cd–Te escape lines (Cd K_{α} escape = 36.3 keV, Cd K_{β} escape = 33.4 keV, Te K_{α} escape = 32 keV) are clearly visible.

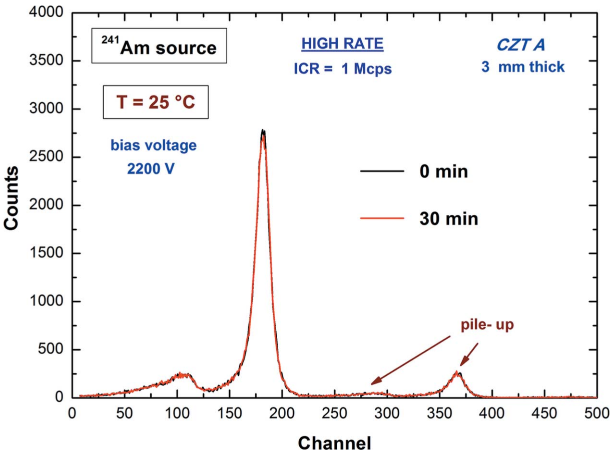

Figure 11
The measured ^{241}Am spectra (ICR = 750 kcounts s^{-1}) of the CZT A detector, just after biasing (black line) and after 30 min (red line). The two lines are not distinguishable, demonstrating the good high-rate stability of the detector. The slow PSHA with ST = 4 µs was used. The Np L X-ray lines, typically of ^{241}Am sources, are shielded by the source holder.

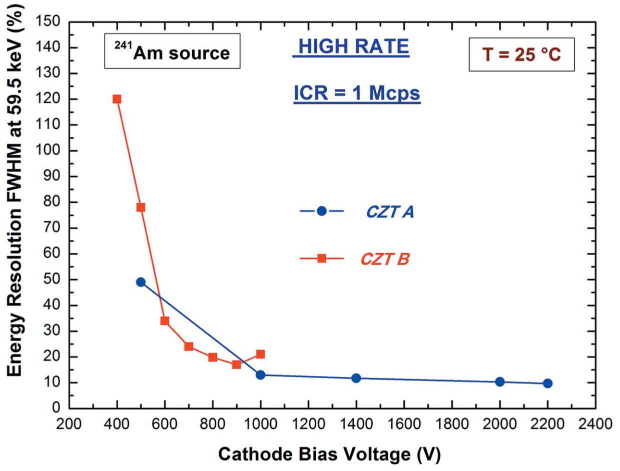

Figure 12
Energy resolution (FWHM) at 59.5 keV (^{241}Am source) *versus* the bias voltage at room temperature for both detectors, at high ICR (1 Mcounts s^{-1}). The slow PSHA with ST = 4 µs was used. The optimal bias voltages are greater than the optimal bias voltages obtained at low rates (Fig. 7). This is due to the effects of the high-flux radiation-induced polarization phenomena, producing a degradation of the electric field within the detectors.

by a charge buildup created within the detector that strongly depends on the radiation characteristics (flux and energy), the detector properties (thickness, bias voltage and charge transport properties) and the operating conditions (temperature). Recently, Bale *et al.* (2008) theoretically investigated the mechanism of the high-flux polarization effects in CZT detectors, obtaining an analytical dependence of the critical flux, above which polarization effects dominate, on material, detector and operating parameters. Polarization degradations are more marked at low temperatures and by increasing the detector thickness and the photon energy; these effects can be mitigated by increasing the bias voltage and by using CZT materials with high charge transport properties (high $\mu_h\tau_h$ values).

As reported in detail in the *Materials and methods* section, the digital system is able to provide two different types of energy spectra: (*a*) energy spectra from the slow PSHA, characterized by a fine energy resolution and a low throughput, and (*b*) energy spectra from the fast PSHA, characterized by poorer energy resolution and high throughput; moreover, both spectra are related to the distribution of the shape of the pulses, expressed through the peaking time (slow PSHA) and the time width (fast PSHA).

At high ICRs, we used the pulse shape to mitigate the pile-up effects in the energy spectra (peak pile-up), as successfully employed in previous works (Abbene & Gerardi, 2011).

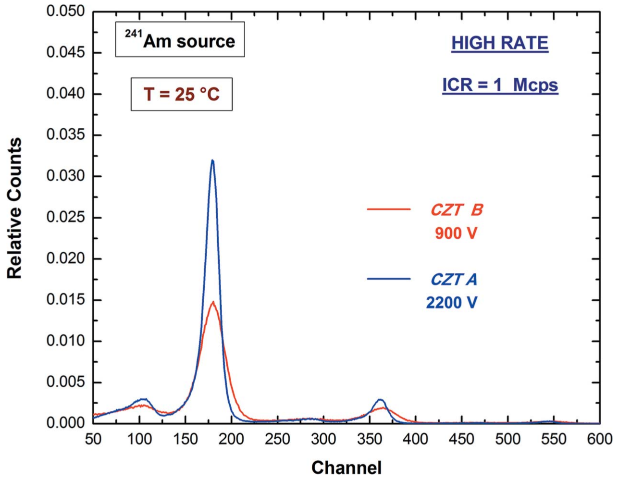

Figure 13
The measured ^{241}Am spectra (ICR = 1 Mcounts s^{-1}) of the CZT detectors. The slow PSHA with ST = 4 µs was used (no PSD). The counts are normalized to the total number of the analyzed events in the spectra. The bias voltages of 900 V and 2200 V allow the best energy resolution values in both detectors: 17% and 9.7% FWHM at 59.5 keV for CZT B and CZT A, respectively.

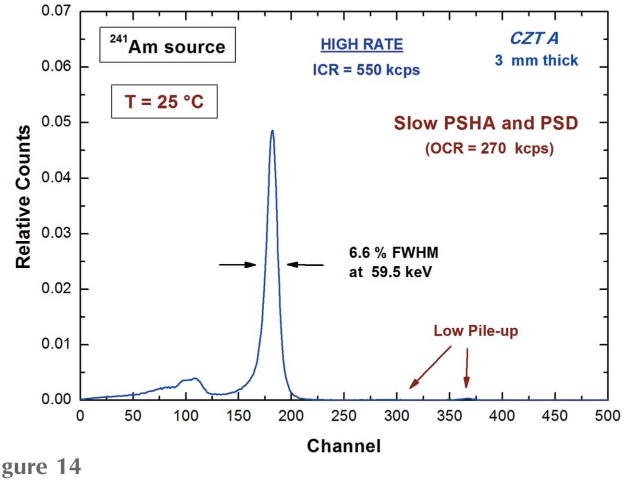

Figure 14
The measured ^{241}Am spectrum (ICR = 550 kcounts s^{-1}) of the CZT A detector, using the slow PSHA (ST = 5 µs) and the PSD. The throughput is 49% and the reduction of pile-up effects, due to the PSD, is clearly visible. The counts are normalized to the total number of the analyzed events in the spectra.

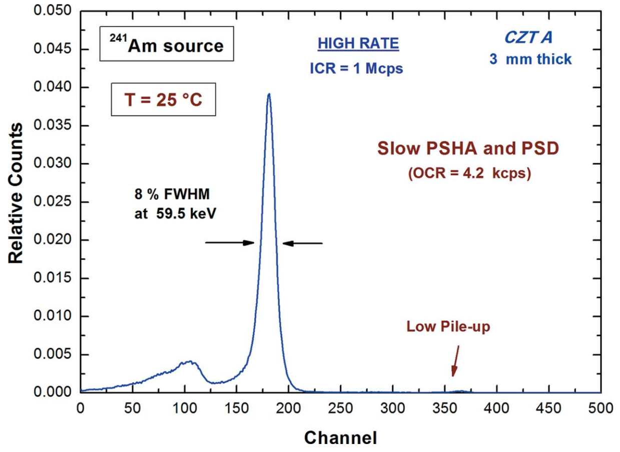

Figure 15
The measured ^{241}Am spectrum (ICR = 1 Mcounts s^{-1}) of the CZT A detector, using the slow PSHA (ST = 5 µs) and the PSD. Despite the excellent energy resolution, a very low throughput of 0.4% characterizes the spectrum. The reduction of pile-up effects, due to the PSD, is clearly visible. The counts are normalized to the total number of the analyzed events in the spectra.

Figs. 14 and 15 show the ^{241}Am spectra measured with the CZT A detector, by using the slow PSHA and the pulse shape discrimination (PSD), at 550 kcounts s^{-1} and at 1 Mcounts s^{-1}, respectively. ^{241}Am (at 1 Mcounts s^{-1}) and ^{57}Co (550 kcounts s^{-1}) spectra, using the fast PSHA and the PSD, are shown in Figs. 16 and 17.

At 1 Mcounts s^{-1}, looking for the optimal energy resolution, the slow PSHA gives, after PSD, better performance (8% FWHM at 59.5 keV) than the fast one (9.7% FWHM at 59.5 keV); whereas, concerning the throughput, the fast PSHA is characterized, even after PSD, by higher throughput (57% after PSD) than the slow one (0.4% after PSD). Table 2 summarizes the high-rate spectroscopic performance of the CZT A detector.

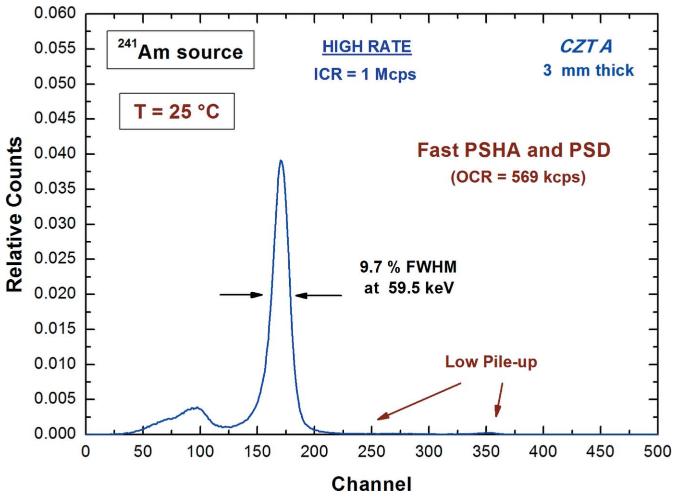

Figure 16
The measured ^{241}Am spectrum (ICR = 1 Mcounts s^{-1}) of the CZT A detector, using the fast PSHA (dead-time = 270 ns) and PSD. Energy resolution values of 9.7% FWHM at 122.1 keV (throughput of 57%) were measured. The reduction of pile-up effects, due to the PSD, is clearly visible. The counts are normalized to the total number of analyzed events in the spectra.

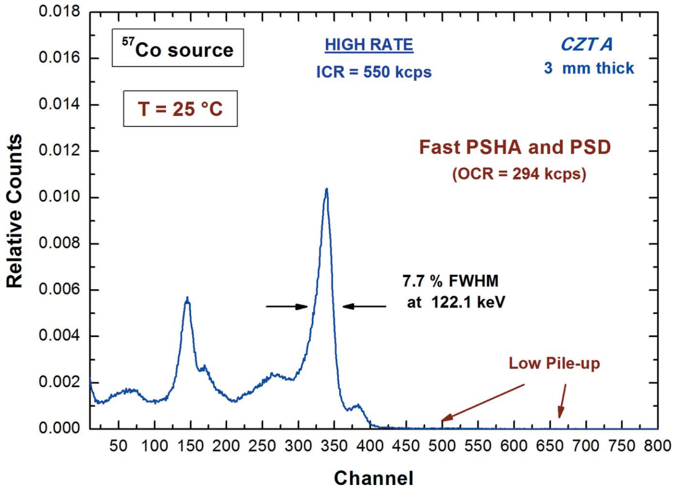

Figure 17
The measured ^{57}Co spectrum (ICR = 550 kcounts s^{-1}) of the CZT A detector, using the fast PSHA (dead-time = 270 ns) and PSD. Energy resolution values of 7.7% FWHM at 122.1 keV (throughput of 53%) were measured. The reduction of pile-up effects, due to the PSD, is clearly visible. The counts are normalized to the total number of analyzed events in the spectra.

Table 2
High-rate (up to 1 Mcounts s^{-1}) spectroscopic performance of the new 3 mm-thick THM-grown CZT detector (CZT A) at T = 25°C.

The digital fast PSHA (dead-time of 270 ns) and the pulse shape discrimination (PSD) were used.

	Energy and ICR	
	59.5 keV at 1 Mcounts s^{-1}	122.1 keV at 550 kcounts s^{-1}
Energy resolution FWHM (%)	9.7	7.7
Throughput (%)	57	53

4. Conclusions

The performance of new THM-grown CZT detectors, developed at IMEM-CNR of Parma (Italy), is presented in this work. The detectors, characterized by low leakage currents even at room temperature, allow high bias voltage operation (>7000 V cm^{-1}, which is very important for high flux radiation measurements.

The detectors, coupled to an innovative digital pulse processing electronics, recently developed at DiFC of University of Palermo (Italy), are characterized by excellent high-rate performance and no high-flux radiation-induced polarization phenomena up to 1 Mcounts s^{-1} (59.5 keV, ^{241}Am source).

The results give important indications on the use of these devices with pixelated electrode structures for high-flux energy-resolved X-ray imaging; *e.g.* a 0.5 mm × 0.5 mm pixel structure (typical of several X-ray imaging applications), based on these CZT detectors, would allow high fluence rates greater than 4 × 10^{6} photons mm^{-2} s^{-1} without excessive spectral distortions.

Ongoing activities are focused on the development of pixelated CZT detectors, with pitches of <0.5 mm, based on these new CZT devices, for room-temperature high-flux energy-resolved X-ray imaging. Charge-sharing effects, through coincidence measurements and pulse-shape analysis, will be investigated.

Acknowledgements

This work was supported by the Italian Ministry for Education, University and Research (MIUR) under PRIN Project No. 2012WM9MEP. The authors would like to acknowledge the technical staff of the laboratory at DiFC of Palermo, Mr Marcello Mirabello, Dr Michele Quartararo and Dr Luigi Tranchina for their technical assistance.

References

Abbene, L. & Gerardi, G. (2011). *Nucl. Instrum. Methods Phys. Res. A*, **654**, 340–348.
Abbene, L. & Gerardi, G. (2015). *J. Synchrotron Rad.* **22**, 1190–1201.
Abbene, L., Gerardi, G. & Principato, F. (2013). *Nucl. Instrum. Methods Phys. Res. A*, **730**, 124–128.

Abbene, L., Gerardi, G. & Principato, F. (2015). *Nucl. Instrum. Methods Phys. Res. A*, **777**, 54–62.

Abbene, L., Gerardi, G., Turturici, A. A., Raso, G., Benassi, G., Bettelli, M., Zambelli, N., Zappettini, A. & Principato, F. (2016). *Nucl. Instrum. Methods Phys. Res. A*, **835**, 1–12.

Auricchio, N., Marchini, L., Caroli, E., Zappettini, A., Abbene, L. & Honkimaki, V. (2011). *J. Appl. Phys.* **110**, 124502.

Awadalla, S. A., Al-Grafi, M. & Iniewski, K. (2014). *Nucl. Instrum. Methods Phys. Res. A*, **764**, 193–197.

Bale, D. S. & Szeles, C. (2008). *Phys. Rev. B*, **77**, 035205.

Barber, W. C., Wessel, J. C., Nygard, E. & Iwanczyk, J. S. (2015). *Nucl. Instrum. Methods Phys. Res. A*, **784**, 531–537.

Baumer, C., Martens, G., Menser, B., Roessl, E., Schlomka, J., Steadman, R. & Zeitler, G. (2008). *IEEE Trans. Nucl. Sci.* **55**, 1785–1790.

Bell, S. J., Baker, M. A., Duarte, D. D., Schneider, A., Seller, P., Sellin, P. J., Veale, M. C. & Wilson, M. D. (2015). *J. Phys. D*, **48**, 275304.

Bertuccio, G., Ahangarianabhari, M., Graziani, C., Macera, D., Shi, Y., Rachevski, A., Rashevskaya, I., Vacchi, A., Zampa, G., Zampa, N., Bellutti, P., Giacomini, G., Picciotto, A. & Piemonte, C. (2015). *J. Instrum.* **10**, P01002.

Bolotnikov, A. E., Boggs, S. E., Hubert Chen, C. M., Cook, W. R., Harrison, F. A. & Schindler, S. M. (2002). *Nucl. Instrum. Methods Phys. Res. A*, **482**, 395–407.

Brambilla, A., Boudou, C., Ouvrier-Buffet, P., Mougel, F., Gonon, G., Rinkel, J. & Verger, L. (2009). *IEEE Nucl. Sci. Symp. Conf. Rec.* pp. 1753–1757.

Brambilla, A., Ouvrier-Buffet, P., Gonon, G., Rinkel, J., Moulin, V., Boudou, C. & Verger, L. (2013). *IEEE Trans. Nucl. Sci.* **60**, 408–415.

Campbell, D. L., Hull, E. L. & Peterson, T. E. (2013). *IEEE Nucl. Sci. Symp. Med. Imaging Conf.* pp. 1–6.

Chaudhuri, S. K., Nguyen, K., Pak, R. O., Matei, L., Buliga, V., Groza, M., Burger, A. & Mandal, K. C. (2014). *IEEE Trans. Nucl. Sci.* **61**, 793–798.

Chen, H., Awadalla, S. A., Iniewski, K., Lu, P. H., Harris, F., Mackenzie, J., Hasanen, T., Chen, W., Redden, R., Bindley, G., Kuvvetli, I., Budtz-Jørgensen, C., Luke, P., Amman, M., Lee, J. S., Bolotnikov, A. E., Camarda, G. S., Cui, Y., Hossain, A. & James, R. B. (2008). *J. Appl. Phys.* **103**, 014903.

Chen, H., Awadalla, S. A., Mackenzie, J., Redden, R., Bindley, G., Bolotnikov, A. E., Camarda, G. S., Carini, G. & James, R. B. (2007). *IEEE Trans. Nucl. Sci.* **54**, 811–816.

Del Sordo, S., Abbene, L., Caroli, E., Mancini, A. M., Zappettini, A. & Ubertini, P. (2009). *Sensors*, **9**, 3491–3526.

Deng, Z., Li, Y. & Liu, Y. (2007). *Nucl. Electron. Detect. Technol.* **27**, 1103–1105.

Fredenberg, E., Lundqvist, M., Cederström, B., Åslund, M. & Danielsson, M. (2010). *Nucl. Instrum. Methods Phys. Res. A*, **613**, 156–162.

Gatti, E. & Rehak, P. (1984). *Nucl. Instrum. Methods Phys. Res.* **225**, 608–614.

Gatti, E., Rehak, P. & Walton, J. T. (1984). *Nucl. Instrum. Methods Phys. Res. A*, **226**, 129–141.

Gerardi, G. & Abbene, L. (2014). *Nucl. Instrum. Methods Phys. Res. A*, **768**, 46–54.

Greenberg, J. A., Hassan, M., Brady, D. J. & Iniewski, K. (2016). *Proc. SPIE*, **9847**, 98470E.

Iniewski, K. (2014). *J. Instrum.* **9**, C11001.

Iwanczyk, J., Nygård, E., Meirav, O., Arenson, J., Barber, W. C., Hartsough, N. E., Malakhov, N. & Wessel, J. C. (2009). *IEEE Trans. Nucl. Sci.* **56**, 535–542.

Johnson, L. C., Ovchinnikov, O., Shokouhi, S. & Peterson, T. E. (2015). *IEEE Trans. Nucl. Sci.* **62**, 2036–2042.

Knoll, G. F. (2000). *Radiation Detection and Measurement*, ch. 4. New York: John Wiley and Sons.

Marchini, L., Zappettini, A., Gombia, E., Mosca, R., Lanata, M. & Pavesi, M. (2009). *IEEE Trans. Nucl. Sci.* **56**, 1823–1826.

Norlin, B., Frojdh, C., Thungstrom, G. & Greiffenberg, D. (2008). *IEEE Nucl. Sci. Symp. Conf. Rec.* pp. 3464–3469.

Owens, A. (2006). *J. Synchrotron Rad.* **13**, 143–150.

Owens, A. & Peacock, A. (2004). *Nucl. Instrum. Methods Phys. Res. A*, **531**, 18–37.

Park, S. H., Ha, J., Lee, J., Cho, Y., Kim, H., Kang, S. & Kim, Y. (2008). *J. Nucl. Sci. Technol.* **45**, 348–351.

Sellin, P. J., Davies, A. W., Lohstroh, A., Ozsan, M. E. & Parkin, J. (2005). *IEEE Trans. Nucl. Sci.* **52**, 3074–3078.

Sellin, P. J., Prekas, G., Franc, J. & Grill, R. (2010). *Appl. Phys. Lett.* **96**, 133509.

Szeles, C., Soldner, S. A., Vydrin, S., Graves, J. & Bale, D. S. (2008). *IEEE Trans. Nucl. Sci.* **55**, 572–582.

Taguchi, K., Frey, E. C., Wang, X., Iwanczyk, J. S. & Barber, W. C. (2010). *Med. Phys.* **37**, 3957–3969.

Taguchi, K. & Iwanczyk, J. S. (2013). *Med. Phys.* **40**, 100901.

Takahashi, T. & Watanabe, S. (2001). *IEEE Trans. Nucl. Sci.* **48**, 950–959.

Tomita, Y., Shirayanagi, Y., Matsui, S., Misawa, M., Takahashi, H., Aoki, T. & Hatanaka, Y. (2004). *IEEE Nucl. Sci. Symp. Conf. Rec.* pp. 3733–3737.

Turturici, A. A., Abbene, L., Gerardi, G., Benassi, G., Bettelli, M., Calestani, D., Zambelli, N., Raso, G., Zappettini, A. & Principato, F. (2016). *Nucl. Instrum. Methods Phys. Res. A*, **830**, 243–250.

Veale, M. C., Bell, S. J., Duarte, D. D., French, M. J., Hart, M., Schneider, A., Seller, P., Wilson, M. D., Kachkanov, V., Lozinskaya, A. D., Novikov, V. A., Tolbanov, O. P., Tyazhev, A. & Zarubin, A. N. (2014). *J. Instrum.* **9**, C12047.

Wu, C. Y. (1982). *J. Appl. Phys.* **53**, 5947–5950.

Zappettini, L., Zha, M., Marchini, L., Calestani, D., Mosca, R., Gombia, E., Zanotti, L., Zanichelli, M., Pavesi, M., Auricchio, N. & Caroli, E. (2009). *IEEE Trans. Nucl. Sci.* **56**, 1743–1746.